Letter

Hyperbolic topological flat bands

Hao Yuan,[*] Weixuan Zhang,[*,†] Qingsong Pei, and Xiangdong Zhang[†]

Key Laboratory of Advanced Optoelectronic Quantum Architecture and Measurements of Ministry of Education, Beijing Key Laboratory of Nanophotonics & Ultrafine Optoelectronic Systems, School of Physics, Beijing Institute of Technology, 100081 Beijing, China

(Received 27 April 2023; revised 3 July 2023; accepted 9 January 2024; published 24 January 2024)

Topological flat bands, which are regarded as the cornerstone of various topological states induced by the many-body interaction, have aroused great interest in the fields of physics and material science. To date, most of the established topological flat bands have been employed in Euclidean space. Here, we report on an observation of hyperbolic topological flat bands in non-Euclidean space. By introducing magnetic flux into the hyperbolic octagon-kagome lattice, energy bands in four-dimensional k space with the nontrivial Chern vector can be created via the formalism of hyperbolic band theory. The bandwidth of hyperbolic topological bands can be significantly reduced by tuning the next-nearest-neighbor coupling strength. Numerical results of finite hyperbolic models with fully and partially open boundary conditions clearly demonstrate the existence of topological boundary states induced by hyperbolic topological flat bands. Moreover, we design and fabricate electric circuits to observe hyperbolic topological flat bands in experiments. Site-resolved impedance responses and robust voltage dynamics demonstrate the coexistence of flat-band dispersion and topological boundary states. This letter may act as a foundation for exploring exotic hyperbolic fractional Chern insulators.

DOI: 10.1103/PhysRevB.109.L041109

Introduction. Flat bands with nontrivial topology have been receiving a lot of attention in recent years and are believed to be key components for the realization of fractional topological states. One pioneering example is the two-dimensional (2D) electron gas in a perpendicular magnetic field, where the flat-band Landau levels with nonzero Chern numbers appear. When a certain fractional number of Landau levels is filled, the system turns into an insulator with nontrivial topology, corresponding to the fractional quantum Hall effect [1–3]. Except for the Landau levels induced by magnetic fields in continuum systems, many investigations have shown that various Abelian and non-Abelian fractional Chern insulators with distinct properties can be realized in tight-binding lattice models with topological flat bands [4–14]. Up to now, the construction of topological flat bands has been widely investigated in different types of lattice models, including a kagome lattice [4], a checkerboard lattice [5,6], the Haldane model on a honeycomb lattice [7–10], a buckled honeycomb lattice [11], and so on. However, to date, all the studies on topological flat-band lattices have been focused on Euclidean space.

On the other hand, the non-Euclidean geometry widely exists in natural and artificial systems [15] and plays important roles in various scientific fields. The recent groundbreaking implementations of 2D hyperbolic lattices in circuit quantum electrodynamics [16] and topolectrical circuits [17] have stimulated numerous advances in hyperbolic physics [18–39]. It is noted that highly degenerated flat bands in hyperbolic lattices have been proposed [16,26,27], where the fraction of flat bands is captured exactly by real-space topology arguments and hyperbolic band theory. Beyond flat-band physics, there are many investigations on the construction of hyperbolic topological states [28–39]. For example, the non-Euclidean analog of the quantum spin Hall effect in hyperbolic lattices has been reported [28]. The boundary-dominated hyperbolic Chern insulator has been theoretically proposed and experimentally fulfilled by electric circuit networks [29]. Furthermore, motivated by the hyperbolic band theory [30–32], hyperbolic topological band insulators with nontrivial first/second Chern numbers and hyperbolic graphene have also been theoretically created and experimentally realized in electric circuits [33–35]. It is important to note that the genus of hyperbolic clusters with periodic boundary conditions grows linearly with the size of the system. In this case, if the hyperbolic topological flat bands living in a large-genus momentum space can be created, the hyperbolic fractional Chern insulators with a large degree of topological ground-state degeneracy are expected to appear. Inspired by these fascinating phenomena and potential interests, it is important to ask whether topological flat bands in hyperbolic lattices exist and how to realize hyperbolic topological flat bands in experiments.

In this letter, we create topological flat bands in non-Euclidean space with a constant negative curvature. By introducing magnetic flux into the hyperbolic octagon-kagome lattice and changing the strength of next-nearest-neighbor (NNN) coupling, the hyperbolic topological flat bands with nontrivial Chern vectors in four-dimensional (4D) k space can be generated. In experiments, the electric circuit is designed and fabricated to observe hyperbolic topological flat bands, where the site-resolved impedance responses and robust

[*]These authors contributed equally to this work.
[†]Corresponding authors: zhangwx@bit.edu.cn; zhangxd@bit.edu.cn

voltage dynamics prove the coexistence of flat-band dispersion and topological boundary states. We suggest a way to engineer topological flat bands in the non-Euclidean space and provide a foundation for exploring exotic hyperbolic fractional Chern insulators.

The theory of hyperbolic topological flat bands. We start to design the 2D hyperbolic lattice model with low-energy topological flat bands. The octagon-kagome lattice, which is the line graph of a regular {8,3} hyperbolic lattice, is considered. Figure 1(a) displays the associated unit cell, which is a regular 8-sided hyperbolic polygon that contains 24 sublattices marked by black dots. Based on the hyperbolic crystalline symmetry, the translational symmetry of a {8,8} hyperbolic tiling exists, where eight translational directions are labeled by γ_1, γ_2, γ_3, γ_4, γ_1^{-1}, γ_2^{-1}, γ_3^{-1}, and γ_4^{-1}. The nearest-neighbor (NN) coupling $t_1 e^{i\varphi}$ and NNN coupling t_2 exist, as illustrated by blue arrow and brown dotted lines. The complex NN couplings can produce the effective magnetic flux of 8φ and 3φ in each octagon and triangle. Using the hyperbolic band theory, our proposed lattice model in 2D hyperbolic space can be described in 4D momentum space k_i ($i = 1, 2, 3, 4$), where phase factors e^{ik_i} along directions given by γ_i ($i = 1, 2, 3, 4$) are introduced. The detailed formalism of the k-space Hamiltonian $H(\mathbf{k})$ is given in Note 1 in the Supplemental Material [40].

Then we calculate hyperbolic Bloch bands in the (k_2, k_3) space with the NNN coupling strength being $t_2 = 0.1$, 0.5, and 1, as shown in Fig. 1(b). Other parameters are set as $k_1 = 0.5\pi$, $k_4 = 0$, $t_1 = 1$, and $\varphi = 0.5\pi$. It is shown that the low-energy bandwidth is significantly changed with different values of t_2. To further clarify this effect, we calculate variations of the low-energy bandwidth (ΔE_b), the size of the lowest band gap (ΔE_g) and the ratio of $\Delta E_b/\Delta E_g$ as a function of t_2, as shown in Figs. 1(c)–1(e). The narrowest bandwidth of low-energy bands and the smallest ratio of $\Delta E_b/\Delta E_g$ appear at $t_2 = 0.5$. Due to the intersection of different hyperbolic bands, a composite Chern number is shared by multiple bands [41]. By calculating composite Chern numbers, we find that low-energy flat bands possess a nontrivial Chern vector of $C = (-1, 1, 1, -1, 1, -1)$, with $C = 1$ ($C = -1$) in 2D sub-torus spanned by two momentum coordinates of (k_3, k_4), (k_1, k_4), (k_1, k_2) [(k_2, k_4), (k_2, k_3), (k_1, k_3)] (see Note 2 in the Supplemental Material [40] for details). It is important to note that hyperbolic topological flat bands can also be generated by tuning the ratio between NN and NNN coupling strengths with other different values of magnetic flux (see Note 3 in the Supplemental Material [40]).

To further illustrate key properties of hyperbolic topological flat bands, we calculate eigenspectra of finite-sized hyperbolic clusters with periodic (Abelian cluster) and partially open boundary conditions, as shown in Figs. 1(f) and 1(g). The color map corresponds to the localization degree of associated eigenstates on boundary lattice sites, whose coordination numbers are less than that of bulk sites. Here, we set $t_1 = 1$, $\varphi = \pi/2$, and $t_2 = 0.5$, and details of hyperbolic cluster are presented in Note 4 in the Supplemental Material [40]. We can see that the eigenspectrum of the hyperbolic model with periodic boundary conditions is matched to hyperbolic Bloch bands, where the low-energy topological flat bands and nontrivial band gaps exist. As for the hyperbolic cluster with

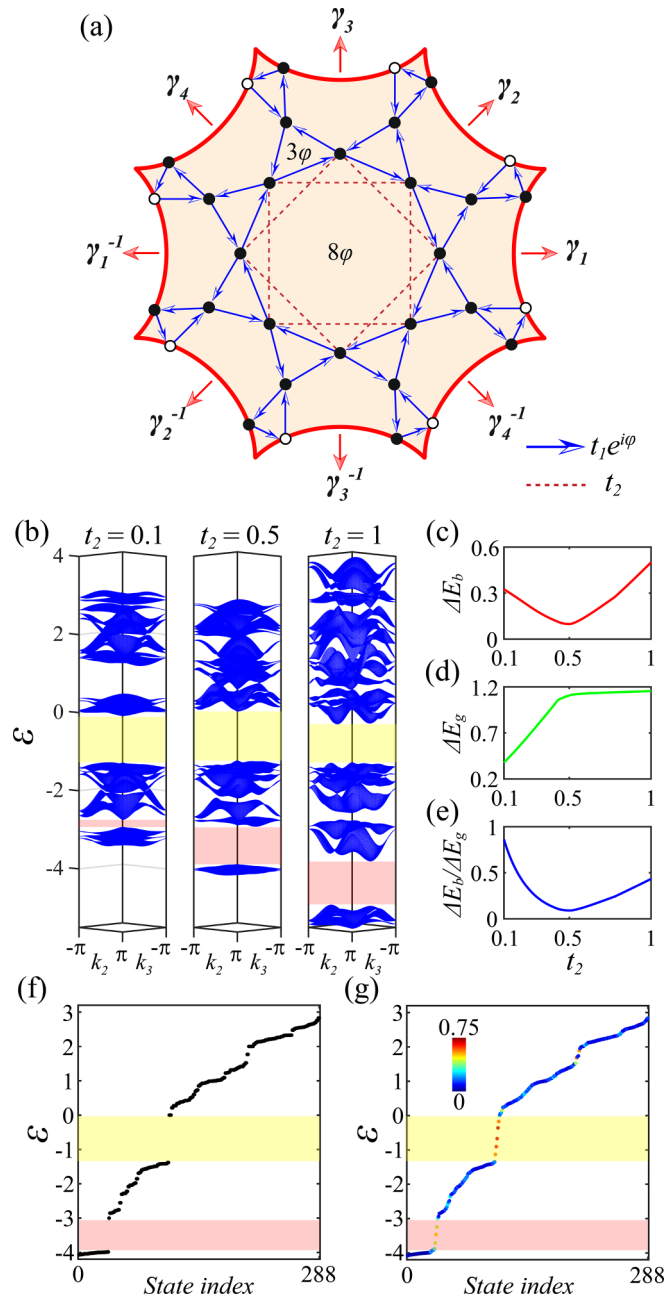

FIG. 1. Topological flat bands in hyperbolic octagon-kagome lattice. (a). The schematic diagram of hyperbolic octagon-kagome lattice with nontrivial topological flat bands. (b). Numerical results of hyperbolic Bloch bands in (k_2, k_3) space with the next-nearest-neighbor (NNN) coupling strength being $t_2 = 0.1$, 0.5, and 1. (c)–(e). Numerical results on variations of ΔE_b, ΔE_g, and $\Delta E_b/\Delta E_g$ as a function of t_2. Other parameters are set as $t_1 = 1$ and $\varphi = 0.5\pi$. (f) and (g) Eigenspectra of finite-sized hyperbolic clusters with periodic and partially open boundary conditions at $t_2 = 0.5$. The color map corresponds to the localization degree of all eigenstates on boundary lattice sites.

partially open boundary conditions, it is shown that midgap boundary states appear in nontrivial band gaps, showing the nontrivial topology of low-energy flat bands.

Now we turn to the planar hyperbolic lattice with open boundary conditions. The calculated energy spectrum is

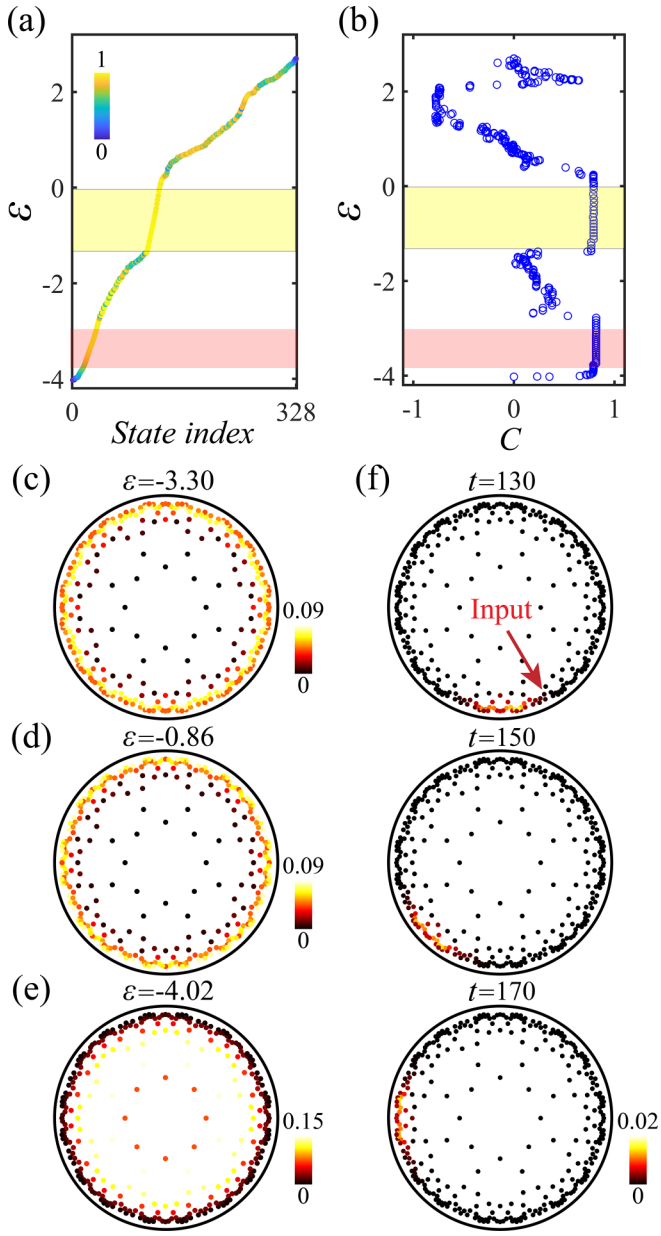

FIG. 2. Topological flat bands and edge states in the octagon-kagome lattice with open boundary condition. (a) and (b) The calculated energy-spectrum and real-space Chern numbers of hyperbolic lattice model with open boundary conditions. (c)–(e). Spatial profiles of eigenmodes with energies being $\varepsilon = -3.30$, -0.86, and -4.02. (f). Time-domain dynamics of hyperbolic lattice model at different times $t = 130$, 150, and 170.

shown in Fig. 2(a). The color map represents the localization of eigenstates on lattice sites at the outermost layer. Figure 2(b) displays the calculated real-space Chern number. We can see that hyperbolic topological states exist in nontrivial energy regions marked by red and yellow blocks, which are matched to topological band gaps evaluated by hyperbolic band theory. To further illustrate the distribution of hyperbolic topological edge states, we plot spatial profiles of eigenmodes with energies being $\varepsilon = -3.30$ and -0.86, as shown in Figs. 2(c) and 2(d). We can see that these midgap eigenmodes possess the significant edge localization, which is a crucial property of nontrivial topological boundary states. In addition, the spatial profile of eigenstate at the flat-band energy of $\varepsilon = -4.02$ is presented in Fig. 2(e), where the probability amplitudes are concentrated in the bulk.

Furthermore, it is widely known that one-way edge states should exist in energy regions with nontrivial real-space Chern numbers. Thus, we numerically investigate the robust evolution of edge states by launching a wave packet $\varphi_{\text{in}}(t) = \exp[-(t-t_0)^2/100]\sin(\varepsilon_c t)$, with $t_0 = 120$ and $\varepsilon_c = -3.30$, into an edge site. Spatial distributions of $|\varphi_i(t)|$ at different times $t = 130$, 150, and 170 are shown in Fig. 2(f). It is clearly shown that the wave packet moves unidirectionally along the edge of the hyperbolic lattice. These numerical results show that the unidirectional edge states exist in the hyperbolic octagon-kagome lattice model.

Experimental observation of hyperbolic topological flat bands in electric circuits. Motivated by recent experimental breakthroughs in topolectrical circuits [42–59], we focus on the design of a hyperbolic electric circuit to observe the hyperbolic topological flat bands. Figure 3(a) illustrates the photograph image of circuit sample, and the inset shows the mapped lattice model. The unit cell of hyperbolic octagon-kagome lattice is enclosed by the red block, where the NN and NNN couplings are illustrated by arrow and dotted lines. Details on the sample fabrication are provided in Note 5 in the Supplemental Material [40]. Here, four circuit nodes connected by capacitors C are considered to form an effective lattice site. Voltages on these four nodes are defined by $V_{i,1}$, $V_{i,2}$, $V_{i,3}$, and $V_{i,4}$, which could be suitably formulated to construct a pair of pseudospins $V_{\uparrow i,\downarrow i} = V_{i,1} \pm iV_{i,2} - V_{i,3} \mp iV_{i,4}$ for realizing required site couplings. Schematic diagrams for the realization of different intercell couplings are shown in Fig. 3(b). To simulate the negative NNN hopping t_2, four capacitors C_2 are used to crossly link adjacent nodes. As for NN couplings with hopping phases $e^{\pm i\pi/2}$, two groups of adjacent nodes are connected crossly via four capacitors C_1. Each circuit node is grounded by an inductor L_g. Through the appropriate setting of grounding and connecting, the circuit eigenequation is identical to that of the hyperbolic octagon-kagome lattice model. The probability amplitude at the lattice site i is mapped to the voltage pseudospin. The effective tight-binding parameters are expressed as $t_1 = C_1/C$, $\varphi = 0.5\pi$, and $t_2 = C_2/C$. The eigenenergy of the hyperbolic lattice model is directly related to the eigenfrequency of electric circuit as $\varepsilon = f_0^2/f^2 - 2 - (4C_1 + 4C_2)/C$, with $f_0 = (2\pi\sqrt{CL_g})^{-1}$. Note 6 in the Supplemental Material [40] provides details on the derivation of the circuit eigenequation. Here, circuit parameters are set as $C = 2nF$, $C_1 = 2nF$, $C_2 = 1nF$, and $L_g = 1\mu H$.

To illustrate the flat-band dispersion, we measure the impedance response of bulk node [the green pentagram in Fig. 3(a)], as shown by the green line in Fig. 3(c). It is shown that there is no impedance peak in frequency ranges of [1.258, 1.383 MHz] and [1.59, 1.776 MHz] (shaded regions), corresponding to the existence of band gaps. There are multiple bulk impedance peaks in two frequency regions of [1, 1.258 MHz] and [1.383, 1.59 MHz] that clearly show energy bands with large widths in $\varepsilon = [1.506, 2.786]$

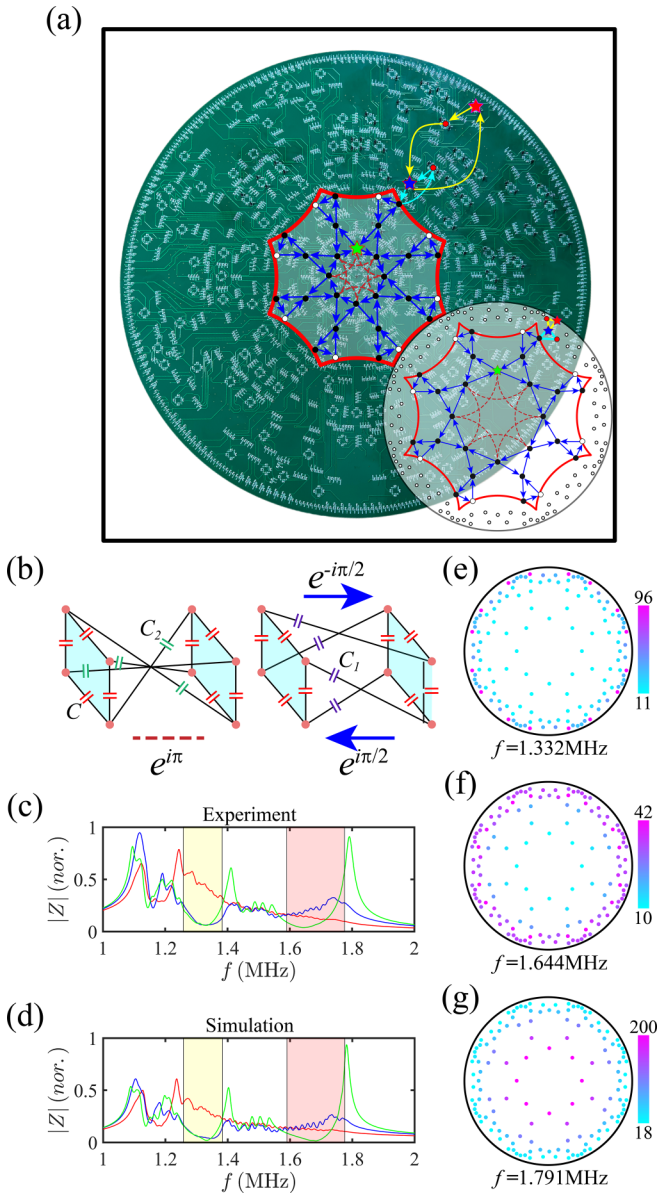

FIG. 3. Impedance responses of topological flat bands and edge states. (a) The photograph image of the circuit sample. The inset shows the mapped lattice model. (b) The schematic diagram for the realization of nearest-neighbor (NN) and next-NN (NNN) couplings. (c) and (d) Measured and simulated impedance responses of bulk (green lines) and edge (red and blue lines) nodes. (e)–(g) The measured spatial impedance distributions at 1.332, 1.644, and 1.791 MHz.

and $[-2.758, -1.342]$. In addition, the bulk node exhibits a large-value impedance peak at 1.791 MHz. The relatively large impedance peaks within an extremely narrow frequency range that is spectrally separated from other eigenfrequencies signify that different bulk modes possess nearly identical eigenfrequencies, thereby confirming their adherence to properties exhibited by flat bands. For comparison purposes, we also compute the impedance responses of bulk nodes for two circuits lacking flat bands (see Note 7 in the Supplemental Material [40] for details). It is evident that more impedance peaks within much wider frequency ranges appear in the high-frequency domain, thereby distinguishing them from the narrow-frequency impedance spectra of flat bands. To further detect the spatial profile of flat bands, we measure the impedance distribution at 1.791 MHz, as presented in Fig. 3(g). It is clearly shown that the spatial profile of impedance is matched to the probability amplitude of a flat-band bulk mode.

Then we turn to the demonstration of nontrivial topological properties of low-energy flat bands. For this purpose, the impedance responses of two edge nodes [red and blue pentagrams in Fig. 3(a)] are measured, as shown by red and blue lines in Fig. 3(c). It is seen that the two edge nodes exhibit significant impedance responses in nontrivial band gaps, manifesting the existence of midgap edge states. Impedances of these two edge nodes possess different amplitudes in two band gaps that result from different local densities of states. Figure 3(d) presents simulation results of impedance responses. A good consistency between simulations and measurements is obtained. To further illustrate spatial profiles of hyperbolic edge states, we measure impedance distributions at 1.332 and 1.644 MHz, as presented in Figs. 3(e) and 3(f). We can see that the spatial impedance profiles are matched to the corresponding edge modes.

Except for the impedance response, we further measure voltage dynamics of bulk and edge nodes to demonstrate the coexistence of the flat-band dispersion and nontrivial topology. Here, four voltage packets, which are expressed as $[V_{i,1}, V_{i,2}, V_{i,3}, V_{i,4}] = [V_0, iV_0, -V_0, -iV_0]\exp[-\frac{(t-t_0)^2}{t_d^2}]\sin(2\pi f_c t)$, are used to excite the voltage pseudospin. Details of experimental technologies are provided in Note 7 in the Supplemental Material [40]. To effectively excite the hyperbolic boundary state, the time delay, packet width, and central frequency of voltage packets are set as $t_0 = 30\,\mu s$, $t_d = 9.69\,\mu s$, and $f_c = 1.642$ MHz, respectively. The frequency spectrum of the injected voltage packet is plotted in Fig. 4(a). It is shown that all frequency components of the input voltage packet are located in the nontrivial region sustaining topological edge states. In this case, the midgap edge state can be dominantly excited by the voltage packet. Figure 4(b) presents the measured time tracks of the voltage pseudospin (normalized to V_0^2) at two edge nodes (red and blue lines) and two bulk nodes (green and black lines) along clockwise and counterclockwise directions. As we can see, the clockwise boundary node possesses a large voltage signal. Meanwhile, voltage signals at the counterclockwise boundary node and two bulk circuit nodes are very small. These experimental results indicate that the voltage packet can propagate unidirectionally along the boundary, ensuring the existence of midgap one-way edge states. This phenomenon demonstrates that the low-energy bulk bands indeed possess nontrivial topology based on the bulk-edge correspondence.

Additionally, it is well known that the flat band can induce the spatial localization within the bulk region due to the zero-valued group velocity of bulk flat bands. To further demonstrate the flat-band effect, a bulk node (marked by pink dot in insets) is excited by three voltage packets with

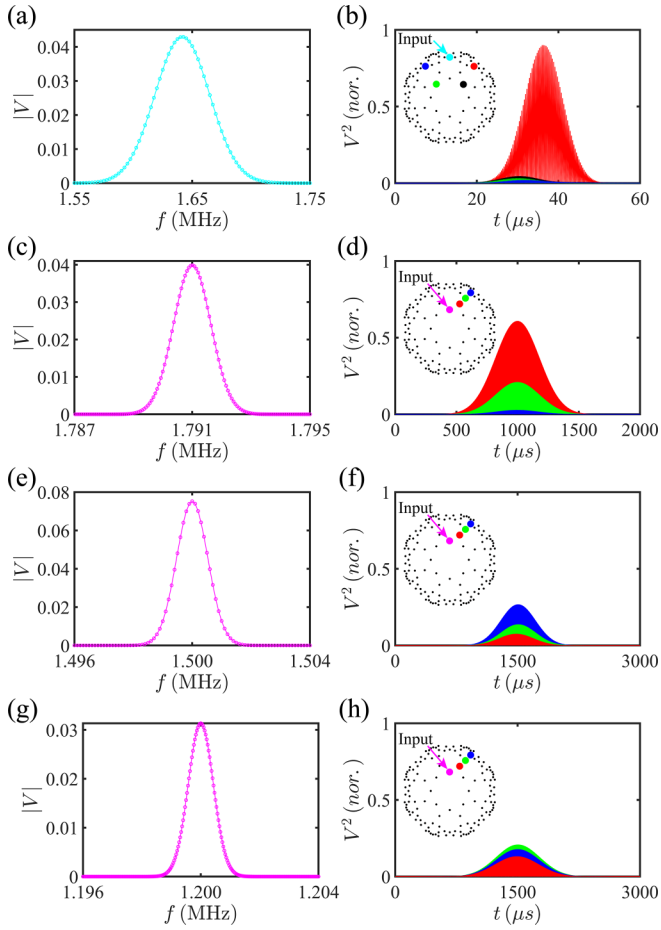

FIG. 4. Observation of the voltage dynamics in the octagon-kagome lattice. (a), (c), (e), and (g) The frequency spectra of injected voltage packets for exciting edge and bulk states. (b), (d), (f), and (h) Measured time tracks of voltage signals at different circuit nodes with exciting the boundary state and flat-band bulk state.

$f_c = 1.791$ MHz ($t_0 = 1$ ms and $t_d = 355$ μs), $f_c = 1.5$ MHz ($t_0 = 1.5$ ms and $t_d = 424$ μs) and $f_c = 1.2$ MHz ($t_0 = 1.5$ ms and $t_d = 531$ μs). The associated frequency spectra are plotted in Figs. 4(c), 4(e), and 4(g). It is shown that the frequency spectra can only cover the low-energy flat band and two high-energy dispersive bands with $f_c = 1.791$, 1.5, and 1.2 MHz. Figures 4(d), 4(f), and 4(h) present experimental dynamics of voltage packets with $f_c = 1.791$, 1.5, and 1.2 MHz. It is shown that the voltage packet is concentrated around the excitation node with $F_c = 1.791$ MHz due to the extremely low group velocity of flat bands. In contrast, the input voltage packet is less concentrated around the input node under the excitation of high-energy dispersive bands.

In conclusion, we have realized topological flat bands in hyperbolic space both in theory and experiments. By introducing the magnetic flux into hyperbolic octagon-kagome lattices and tuning the strength of NNN couplings, hyperbolic topological flat bands with a nontrivial Chern vector can be generated. Numerical results clearly show that topological boundary states appear in finite hyperbolic lattices with fully and partially open boundaries. In experiments, we have designed and fabricated electric circuits to detect hyperbolic topological flat bands, where the site-resolved impedance responses and robust voltage dynamics demonstrate the coexistence of flat-band dispersion and topological boundary states. In this letter, we suggest a way to engineer topological flat bands in non-Euclidean space, which may provide a foundation for exploring hyperbolic fractional Chern insulators.

Acknowledgments. This letter is supported by the National Key R & D Program of China Grant No. 2022YFA1404900, Young Elite Scientists Sponsorship Program by CAST Grant No. 2023QNRC001, the National Natural Science Foundation of China Grant No. 12104041, and the BIT Research and Innovation Promoting Project No. 2022YCXZ027.

[1] D. C. Tsui, H. L. Stormer, and A. C. Gossard, Two-dimensional magnetotransport in the extreme quantum limit, Phys. Rev. Lett. **48**, 1559 (1982).
[2] R. B. Laughlin, Anomalous quantum Hall effect: An incompressible quantum fluid with fractionally charged excitations, Phys. Rev. Lett. **50**, 1395 (1983).
[3] H. L. Stormer, D. C. Tsui, and A. C. Gossard, The fractional quantum Hall effect, Rev. Mod. Phys. **71**, S298 (1999).
[4] E. Tang, J.-W. Mei, and X.-G. Wen, High-temperature fractional quantum Hall states, Phys. Rev. Lett. **106**, 236802 (2011).
[5] D. N. Sheng, Z.-C. Gu, K. Sun, and L. Sheng, Fractional quantum Hall effect in the absence of Landau levels, Nat. Commun. **2**, 389 (2011).
[6] K. Sun, Z. Gu, H. Katsura, and S. Das Sarma, Nearly flatbands with nontrivial topology, Phys. Rev. Lett. **106**, 236803 (2011).
[7] Y.-L. Wu, B. A. Bernevig, and N. Regnault, Zoology of fractional Chern insulators, Phys. Rev. B **85**, 075116 (2012).
[8] T. Neupert, L. Santos, C. Chamon, and C. Mudry, Fractional quantum Hall states at zero magnetic field, Phys. Rev. Lett. **106**, 236804 (2011).
[9] Y.-F. Wang, Z.-C. Gu, C.-D. Gong, and D. N. Sheng, Fractional quantum Hall effect of hard-core bosons in topological flat bands, Phys. Rev. Lett. **107**, 146803 (2011).
[10] N. Regnault and B. A. Bernevig, Fractional Chern insulator, Phys. Rev. X **1**, 021014 (2011).
[11] D. Xiao, W. Zhu, Y. Ran, N. Nagaosa, and S. Okamoto, Interface engineering of quantum Hall effects in digital transition metal oxide heterostructures, Nat. Commun. **2**, 596 (2011).
[12] J. W. F. Venderbos, S. Kourtis, J. van den Brink, and M. Daghofer, Fractional quantum-Hall liquid spontaneously generated by strongly correlated t_{2g} electrons, Phys. Rev. Lett. **108**, 126405 (2012).
[13] E. J. Bergholtz and Z. Liu, Topological flat band models and fractional Chern insulators, Int. J. Mod. Phys. B **27**, 1330017 (2013).
[14] T. Neupert, C. Chamon, T. Iadecola, L. H. Santos, and C. Mudry, Fractional (Chern and topological) insulators, Phys. Scr. **2015**, 014005 (2015).
[15] W. Magnus, *Noneuclidean Tesselations and Their Groups* (Academic Press, New York, 1974).

[16] A. J. Kollar, M. Fitzpatrick, and A. A. Houck, Hyperbolic lattices in circuit quantum electrodynamics, Nature (London) **571**, 45 (2019).

[17] P. M. Lenggenhager, A. Stegmaier, L. K. Upreti, T. Hofmann, T. Helbig, A. Vollhardt, M. Greiter, C. H. Lee, S. Imhof, H. Brand *et al.*, Simulating hyperbolic space on a circuit board, Nat. Commun. **13**, 4373 (2022).

[18] P. Basteiro, F. Dusel, J. Erdmenger, D. Herdt, H. Hinrichsen, R. Meyer, and M. Schrauth, Breitenlohner-Freedman bound on hyperbolic tilings, Phys. Rev. Lett. **130**, 091604 (2023).

[19] I. Boettcher, P. Bienias, R. Belyansky, A. J. Kollar, and A. V. Gorshkov, Quantum simulation of hyperbolic space with circuit quantum electrodynamics: From graphs to geometry, Phys. Rev. A **102**, 032208 (2020).

[20] A. J. Kollar, M. Fitzpatrick, P. Sarnak, and A. A. Houck, Line-graph lattices: Euclidean and non-Euclidean flat bands, and implementations in circuit quantum electrodynamics, Commun. Math. Phys **376**, 1909 (2020).

[21] K. Ikeda, S. Aoki, and Y. Matsuki, Hyperbolic band theory under magnetic field and Dirac cones on a higher genus surface, J. Phys. Condens. Matter **33**, 485602 (2021).

[22] P. Bienias, I. Boettcher, R. Belyansky, A. J. Kollar, and A. V. Gorshkov, Circuit quantum electrodynamics in hyperbolic space: From photon bound states to frustrated spin models, Phys. Rev. Lett. **128**, 013601 (2022).

[23] N. Cheng, F. Serafin, J. McInerney, Z. Rocklin, K. Sun, and X. Mao, Band theory and boundary modes of high-dimensional representations of infinite hyperbolic lattices, Phys. Rev. Lett. **129**, 088002 (2022).

[24] A. Attar and I. Boettcher, Selberg trace formula in hyperbolic band theory, Phys. Rev. E **106**, 034114 (2022).

[25] X. Zhu, J. Guo, N. P. Breuckmann, H. Guo, and S. Feng, Quantum phase transitions of interacting bosons on hyperbolic lattices, J. Phys. Condens. Matter **33**, 335602 (2021).

[26] T. Bzdusek and J. Maciejko, Flat bands and band-touching from real-space topology in hyperbolic lattices, Phys. Rev. B **106**, 155146 (2022).

[27] R. Mosseri, R. Vogeler, and J. Vidal, Aharonov-Bohm cages, flat bands, and gap labeling in hyperbolic tilings, Phys. Rev. B **106**, 155120 (2022).

[28] S. Yu, X. Piao, and N. Park, Topological hyperbolic lattices, Phys. Rev. Lett. **125**, 053901 (2020).

[29] W. Zhang, H. Yuan, N. Sun, H. Sun, and X. Zhang, Observation of novel topological states in hyperbolic lattices, Nat. Commun. **13**, 2937 (2022).

[30] J. Maciejko and S. Rayan, Hyperbolic band theory, Sci. Adv. **7**, eabe9170 (2021).

[31] J. Maciejko and S. Rayan, Automorphic Bloch theorems for hyperbolic lattices, Proc. Natl Acad. Sci. USA **119**, e2116869119 (2022).

[32] I. Boettcher, A. V. Gorshkov, A. J. Kollar, J. Maciejko, S. Rayan, and R. Thomale, Crystallography of hyperbolic lattices, Phys. Rev. B **105**, 125118 (2022).

[33] D. M. Urwyler, P. M. Lenggenhager, I. Boettcher, R. Thomale, T. Neupert, and T. Bzdusek, Hyperbolic topological band insulators, Phys. Rev. Lett. **129**, 246402 (2022).

[34] W. Zhang, F. Di, X. Zheng, H. Sun, and X. Zhang, Hyperbolic band topology with non-trivial second Chern numbers, Nat. Commun. **14**, 1083 (2023).

[35] A. Chen, H. Brand, T. Helbig, T. Hofmann, S. Imhof, A. Fritzsche, T. Kießling, A. Stegmaier, L. K. Upreti, T. Neupert *et al.*, Hyperbolic matter in electrical circuits with tunable complex phases, Nat. Commun. **14**, 622 (2023).

[36] Z.-R. Liu, C.-B. Hua, T. Peng, and B. Zhou, Chern insulator in a hyperbolic lattice, Phys. Rev. B **105**, 245301 (2022).

[37] A. Stegmaier, L. K. Upreti, R. Thomale, and I. Boettcher, Universality of Hofstadter butterflies on hyperbolic lattices, Phys. Rev. Lett. **128**, 166402 (2022).

[38] Z.-R. Liu, C.-B. Hua, T. Peng, R. Chen, and B. Zhou, Higher-order topological insulators in hyperbolic lattices, Phys. Rev. B **107**, 125302 (2023).

[39] Y.-L. Tao and Y. Xu, Higher-order topological hyperbolic lattices, Phys. Rev. B **107**, 184201 (2023).

[40] See Supplemental Material at http://link.aps.org/supplemental/10.1103/PhysRevB.109.L041109 for details on the k-space hyperbolic Hamiltonian and topological flat bands at different values of magnetic flux, the eigenequation of hyperbolic electric circuits, and experimental methods.

[41] R. Zhao, G.-D. Xie, M. L. N. Chen, Z. Lan, Z. Huang, and W. E. I. Sha, First-principle calculation of Chern number in gyrotropic photonic crystals, Opt. Express **28**, 4638 (2020).

[42] J. Ningyuan, C. Owens, A. Sommer, D. Schuster, and J. Simon, Time- and site-resolved dynamics in a topological circuit, Phys. Rev. X **5**, 021031 (2015).

[43] V. V. Albert, L. I. Glazman, and L. Jiang, Topological properties of linear circuit lattices, Phys. Rev. Lett. **114**, 173902 (2015).

[44] C. H. Lee, S. Imhof, C. Berger, F. Bayer, J. Brehm, L. W. Molenkamp, T. Kiessling, and R. Thomale, Topolectrical circuits, Commun. Phys. **1**, 39 (2018).

[45] S. Imhof, C. Berger, F. Bayer, J. Brehm, L. W. Molenkamp, T. Kiessling, F. Schindler, C. H. Lee, M. Greiter, T. Neupert *et al.*, Topolectrical-circuit realization of topological corner modes, Nature Phys. **14**, 925 (2018).

[46] T. Helbig, T. Hofmann, C. H. Lee, R. Thomale, S. Imhof, L. W. Molenkamp, and T. Kiessling, Band structure engineering and reconstruction in electric circuit networks, Phys. Rev. B **99**, 161114(R) (2019).

[47] Y. Wang, H. M. Price, B. Zhang, and Y. D. Chong, Circuit implementation of a four-dimensional topological insulator, Nat. Commun. **11**, 2356 (2020).

[48] N. A. Olekhno, E. I. Kretov, A. A. Stepanenko, P. A. Ivanova, V. V. Yaroshenko, E. M. Puhtina, D. S. Filonov, B. Cappello, L. Matekovits, and M. A. Gorlach, Topological edge states of interacting photon pairs emulated in a topolectrical circuit, Nat. Commun. **11**, 1436 (2020).

[49] W. Zhang, D. Zou, Q. Pei, W. He, J. Bao, H. Sun, and X. Zhang, Experimental observation of higher-order topological Anderson insulators, Phys. Rev. Lett. **126**, 146802 (2021).

[50] M. Di Ventra, Y. V. Pershin, and C.-C. Chien, Custodial chiral symmetry in a Su-Schrieffer-Heeger electrical circuit with memory, Phys. Rev. Lett. **128**, 097701 (2022).

[51] S. S. Yamada, T. Li, M. Lin, C. W. Peterson, T. L. Hughes, and G. Bahl, Bound states at partial dislocation defects in multipole higher-order topological insulators, Nat. Commun. **13**, 2035 (2022).

[52] J. Wu, Z. Wang, Y. Biao, F. Fei, S. Zhang, Z. Yin, Y. Hu, Z. Song, T. Wu, F. Song *et al.*, Non-Abelian gauge fields in circuit systems, Nat. Electron. **5**, 635 (2022).

[53] R. Li, B. Lv, H. Tao, J. Shi, Y. Chong, B. Zhang, and H. Chen, Ideal type-II Weyl points in topological circuits, Natl. Sci. Rev. **8**, nwaa192 (2021).

[54] S. Liu, R. Shao, S. Ma, L. Zhang, O. You, H. Wu, Y. J. Xiang, T. J. Cui, and S. Zhang, Non-Hermitian skin effect in a non-Hermitian electrical circuit, Research **2021**, 5608038 (2021).

[55] B. Lv, R. Chen, R. Li, C. Guan, B. Zhou, G. Dong, C. Zhao, Y. Li, Y. Wang, H. Tao *et al.*, Realization of quasicrystalline quadrupole topological insulators in electrical circuits, Commun. Phys. **4**, 126 (2021).

[56] L. Song, H. Yang, Y. Cao, and P. Yan, Square-root higher-order Weyl semimetals, Nat. Commun. **13**, 5601 (2022).

[57] Z. Wang, X.-T. Zeng, Y. Biao, Z. Yan, and R. Yu, Realization of a Hopf insulator in circuit systems, Phys. Rev. Lett. **130**, 057201 (2023).

[58] H. Yang, L. Song, Y. Cao, and P. Yan, Experimental realization of two-dimensional weak topological insulators, Nano Lett. **22**, 3125 (2022).

[59] W. Zhang, H. Wang, H. Sun, and X. Zhang, Non-Abelian inverse Anderson transitions, Phys. Rev. Lett. **130**, 206401 (2023).